PLOS ONE

RESEARCH ARTICLE

# Robustness of common hemodynamic indicators with respect to numerical resolution in 38 middle cerebral artery aneurysms

**Øyvind Evju[1], Jose M. Pozo[2], Alejandro F. Frangi[2], Kent-Andre Mardal[1,3]***

**1** Center for Biomedical Computing, Simula Research Laboratory, Oslo, Norway, **2** Centre for Computational Imaging & Simulation Technologies in Biomedicine (CISTIB), Department of Electronic and Electrical Engineering, University of Sheffield, Sheffield, United Kingdom, **3** Department of Mathematics, University of Oslo, Oslo, Norway

* kent-and@math.uio.no





**Citation:** Evju Ø, Pozo JM, Frangi AF, Mardal K-A (2017) Robustness of common hemodynamic indicators with respect to numerical resolution in 38 middle cerebral artery aneurysms. PLoS ONE 12(6): e0177566. https://doi.org/10.1371/journal.pone.0177566

**Editor:** Josué Sznitman, Technion Israel Institute of Technology, ISRAEL

**Received:** July 8, 2016

**Accepted:** April 28, 2017

**Published:** June 13, 2017



**Data Availability Statement:** The minimal underlying data set necessary for replication of this study is within Figshare: http://dx.doi.org/10.15131/shef.data.4806910.

**Funding:** This work was funded by Norwegian Research Council grant 179578, http://www.forskningsradet.no (ØE, KAM); Norwegian Research Council grant 251237, http://www.forskningsradet.no (ØE, KAM). This work was partially funded from the European Union Sixth Framework Programme (FP6) in the context of the

## Abstract

### Background

Using computational fluid dynamics (CFD) to compute the hemodynamics in cerebral aneurysms has received much attention in the last decade. The usability of these methods depends on the quality of the computations, highlighted in recent discussions. The purpose of this study is to investigate the convergence of common hemodynamic indicators with respect to numerical resolution.

### Methods

38 middle cerebral artery bifurcation aneurysms were studied at two different resolutions (one comparable to most studies, and one finer). Relevant hemodynamic indicators were collected from two of the most cited studies, and were compared at the two refinements. In addition, correlation to rupture was investigated.

### Results

Most of the hemodynamic indicators were very well resolved at the coarser resolutions, correlating with the finest resolution with a correlation coefficient >0.95. The oscillatory shear index (OSI) had the lowest correlation coefficient of 0.83. A logarithmic Bland-Altman plot revealed noticeable variations in the proportion of the aneurysm under low shear, as well as in spatial and temporal gradients not captured by the correlation alone.

### Conclusion

Statistically, hemodynamic indicators agree well across the different resolutions studied here. However, there are clear outliers visible in several of the hemodynamic indicators, which suggests that special care should be taken when considering individual assessment.

Integrated Project @neurIST: Integrated Biomedical Informatics for the Management of Cerebral Aneurysms (IST-2005-027703). The funders had no role in study design, data collection and analysis, decision to publish, or preparation of the manuscript.

**Competing interests:** The authors have declared that no competing interests exist.

**Abbreviations:** AR, Aspect ratio; AWSS, average WSS; CFD, Computational fluid dynamics; ICI, Inflow concentration index; MWSS, Maximal WSS; LSA, Low shear area; NSI, Non-sphericity index; OSI, Oscillatory shear index; SCI, Shear concentration index; TDWSS, Time-derivative of WSS; VDR, Viscous dissipation ratio; WSS, Wall shear stress; WSSG, WSS gradient.

## Introduction

Unruptured aneurysms constitute a major dilemma for clinicians because of the high prevalence of about 2%, the low annual rupture risk of less than 1%, combined with a high mortality of around 40% associated with rupture [1,2]. For this reason, improved risk assessment is sought to improve treatment and reduce costs. To this end, several indicators representing aneurysm morphology [3–8] and hemodynamics [9–14] have been proposed as biomarkers for aneurysm rupture.

The in vivo measurement of detailed blood flow in intracranial aneurysms is currently infeasible, since the existing methods are invasive and/or too limited in resolution. Because of this, computational fluid dynamics (CFD) have been used to estimate the blood flow in aneurysms and adjacent vessels. However, methods, resolutions, models and hemodynamic indicators vary among studies and confound clinicians [15], and thus, CFD is still not widely considered or used in clinical settings. For instance, the ASME 2012 Challenge [16] displayed significant variations among results obtained from different research groups despite a common surface geometry and flow rate conditions (boundary conditions and mesh varied among the groups). Furthermore, deviation from laminar flow has been observed [17,18]. These studies have spurred significant activity on qualitative assessment of the effect of numerical schemes, software packages and resolution [19–22]. Our motivation with the current study is to address whether resolution plays an important role in quantitative studies. In particular, the velocity and pressure are not the main quantities of interest. Hemodynamic indicators often involve integration and differentiation of velocity and/or pressure in both space and time. From a theoretical point of view, such derived quantities converge at different rates than velocity and pressure, in particular, convergence is often decreased by differentiation and gained by integration.

In the numerous CFD studies on cerebral aneurysms available, a wide range of hemodynamic indicators has been proposed. Most are based on the wall shear stress (WSS), that is, the friction acting on the vessel wall, which may vary considerably both with respect to location, phase in the cardiac cycle, and among patients. Some indicators like maximal or average WSS are motivated by the assumption that the vessels are only able to sustain a certain amount of friction. Others, like oscillatory shear index (OSI), low shear area (LSA), WSS gradients (WSSG), and shear concentration index (SCI) are more directly motivated by the mechanotransduction in the vessel walls. Other indicators attempt to quantify the dissipation or jets in the flow like the viscous dissipation ratio (VDR) and inflow concentration index (ICI). The convergence or sensitivity with respect to resolution, methods and models may vary among these indicators. In [19], the authors highlight the missing or inadequate convergence tests in computational studies. The cause of this is suggested to be the computational time required, but they also point to choice of numerical scheme, with schemes tailored for laminar flow might never capture transitional or turbulent flow patterns. Furthermore, the relationship between the different indicators has been highlighted for being insufficiently discussed [15].

In this study, we have investigated the robustness of common hemodynamic indicators with respect to numerical resolution. We have chosen indicators from two of the most frequently cited studies in the field, namely Cebral et al. [10] and Xiang et al. [14]. From these studies, all hemodynamic indicators significantly correlated with rupture state ($p<0.05$), were computed. In addition, we computed the wall shear stress gradient (WSSG) and the wall shear stress time derivative (TDWSS) for completeness, in order to capture spatial and temporal variations. We computed all indicators at different refinement levels to investigate the effects of numerical resolution. Finally, we also included the morphological indicators aspect ratio (AR), non-sphericity index (NSI) and volume (V). Correlations among morphological indicators,

hemodynamic indicators, and rupture status were investigated to uncover potential surrogates. To limit the amount of variability in the data selection, we limited our study to middle cerebral artery (MCA) bifurcation aneurysms. A total of 38 geometries were studied.

## Methods

3D Rotational Angiography (3DRA) images from 53 patients including a MCA bifurcation aneurysm were selected from the @neurIST [23,24] database. The cerebral vasculature in the region of interest was automatically segmented by a geodesic active region segmentation method [25]. The possible geometrical and topological errors in the resulting vessel surface were manually corrected using the suite @neuFuse [24]. The vasculature of interest was isolated cutting with planes perpendicular to the centerline, and the neck was manually delineated as the surface separating the aneurysm dome from the parent vessels, instead of a single plane [7].

A selection of the suitable geometries was made based on the sufficient length of the vessels present on the segmentation. Geometries where the segmentation did not reach further upstream than the C3 segment of the internal carotid artery (ICA) were excluded from further analysis. This was done to include possible secondary flows initiated around the carotid siphon that propagates downstream, as noted in [26]. In the cases where we had multiple segmentations, the geometry with the longest centerline was selected. A total of 38 geometries were included for further studies, and shown in S1 Fig. A brief summary of the selected dataset is found in Table 1.

The hemodynamic indicators computed include the ones significantly correlated with aneurysm rupture state in either Xiang et al. [14] or Cebral et al. [10]. In addition, the wall shear stress gradient and a wall shear stress time derivative functional are computed for completeness. The exact definitions and significance of each of the indicators computed, are shown in Table 2 and Table 3.

For completeness, we have also included in the study the two morphological indicators most frequently considered [6,7,14] for their high correlation with aneurysm rupture state: aspect ratio (AR) [27] and non-sphericity index (NSI) [4]. Their definition is presented in Table 4, and they were automatically computed from the segmented aneurysm surface and the delineated neck. We have also included the aneurysm volume as size indicator.

Tetrahedral meshes were generated using VMTK (www.vmtk.org). We generated two sets of meshes to investigate the robustness of the computed indicators with respect to numerical resolution. We varied the resolution depending proximity to the aneurysm domain, increasing the target nodal distance up to a factor 2 furthest from the aneurysm domain. The parent artery had a target nodal distance of 1.25 times the intra-aneurysmal target nodal distance. For small arteries, we reverted to a radius-adaptive sizing method. All meshes included a boundary layer of approximately 0.3 times the target nodal distance. This boundary layer consisted of 4 sublayers, gradually decreasing in thickness by a factor 0.6, resulting in the outermost sublayer to be of an approximate thickness of 0.03 times the target nodal distance.

**Table 1. Summary of the selected dataset.**

| Parameter | Data range |
|---|---|
| *Ruptured/unruptured* | *13/25* |
| *Age [years]* | *35–78 ($\mu$ = 52.8, $\sigma$ = 9.2)* |
| *Female/male [–]* | *28/10* |
| *Flow rate (ICA) [ml/min]* | *100–382 ($\mu$ = 245, $\sigma$ = 62)* |
| *Flow rate (MCA) [ml/min]* | *58–255 ($\mu$ = 134, $\sigma$ = 38)* |

https://doi.org/10.1371/journal.pone.0177566.t001

**Table 2. Definition of computed hemodynamic indicators from literature.** For notation, we refer the reader to S1 Table.

| Indicator | Abbrev. | Study | Significance | Definition used |
|---|---|---|---|---|
| *Time- and space-averaged WSS* | *AWSS* | *Xiang et al. [14]* | *R<U (p<0.0001)* | $\frac{1}{A_a}\int_{\Gamma_a} \lvert\bar{\tau}\rvert dS$ |
| *Maximum WSS* | *MWSS* | *Xiang et al. [14] Cebral et al. [10]* | *R<U (p = 0.0002) R>U (p<0.004)* | $\max_{x\in\Gamma_a} \lvert\bar{\tau}\rvert$ |
| *Oscillatory shear index* | *OSI* | *Xiang et al. [14]* | *R>U (p<0.0001)* | $\frac{1}{A_a}\int_{\Gamma_a} \frac{1}{2}\left(1-\frac{\lvert\bar{\tau}\rvert}{\lvert\tau\rvert}\right) dS$ |
| *Low shear area* | *LSA* | *Xiang et al. [14]* | *R>U (p<0.0001)* | $\frac{1}{A_a}\int_{\Gamma_a} \begin{cases} 1, & if(\bar{\tau}) < 0.1AWSS \\ 0, & otherwise \end{cases} dS$ |
| *Viscous dissipation ratio* | *VDR* | *Cebral et al. [10]* | *R<U (p<0.0174)* | $\frac{1}{T1-T0}\int_{T0}^{T1} \frac{\frac{1}{V_a}\int_{\Omega_a} 2\frac{\mu}{\rho}\lvert\epsilon\rvert^2 dV}{\frac{1}{V_{nv}}\int_{\Omega_{nv}} 2\frac{\mu}{\rho}\lvert\epsilon\rvert^2 dV} dt$ |
| *Inflow concen-tration index* | *ICI* | *Cebral et al. [10]* | *R>U (p<0.004)* | $\frac{1}{T1-T0}\int_{T0}^{T1} \frac{Q_{in}/Q_{pa}}{A_{in}/A_{neck}} dt$ |
| *Shear concen-tration index* | *SCI* | *Cebral et al. [10]* | *R>U (p<0.049)* | $\frac{1}{T1-T0}\int_{T0}^{T1} \frac{F_h/F_a}{A_h/A_a} dt$ |

https://doi.org/10.1371/journal.pone.0177566.t002

The coarse meshes were motivated by other studies in the field, limited by the resolution required to resolve the geometry. These consisted of 0.5–1.5 million cells, with an average nodal distance of 0.18mm close to the aneurysm domain, increasing to the double further from the aneurysm. The resolution of the finer meshes used was motivated by the resolutions given in Valen-Sendstad and Steinman [19], and had an average nodal distance of 0.13mm in the near-aneurysm domain. The velocity is approximated using piecewise quadratic polynomials, making the effective mesh resolution 0.065mm. The meshes varied in size from 1.2 to 4.0 million cells. This corresponds to approximately 10–32 million linear elements. Compared to Valen-Sendstad and Steinman [19], our fine spatial resolution is similar to their high resolution (0.065mm to 0.06mm). The coarse meshes are approximately 50% coarser than their normal resolution (0.18mm to 0.12mm), and comparable to the resolution in [10,28]. A comparison of the two refinements is visualized in Fig 1.

By selecting 8000 time steps for the coarse mesh, and 23000 time steps for the fine mesh, we assured the same Courant number for both refinements, which is below 1 for flow velocities up to 1.5 m/s.

All hemodynamic indicators were computed on both sets of refinements, and compared with correlation coefficients, average differences and a Bland-Altman plot [29]. Differences between indicators were calculated globally, that is as the difference in global magnitude, rather than the magnitude of the difference locally. A more comprehensive test was performed on the five first aneurysms of the dataset, where all results were computed on 4 different resolutions. The 2 additional meshes had a resolution between the coarse and the fine meshes. For all resolutions, the velocity was approximated with piecewise quadratic polynomials, and the indicators were computed from the second cycle.

We assume blood to behave as a Newtonian fluid with a dynamic viscosity (μ) of 3.45 mPa s, as justified by Evju et al. [30], and with a density of 1.056 g/mm$^3$ (ρ). The walls were assumed to be rigid and impermeable. The inflow boundary conditions were set on the C2/C3 segment as a Womersley profile [31] scaled with the cross-sectional area, as suggested in[32]. The

**Table 3. Definition of computed hemodynamic indicators added for completion.**

| Indicator | Abbrev. | Definition used |
|---|---|---|
| *Time-derivative WSS* | *TDWSS* | $\frac{1}{A_a}\int_{\Gamma_a} \lvert\overline{\frac{\partial\lvert\tau\rvert}{\partial t}}\rvert dS$ |
| *WSS gradient* | *WSSG* | $\frac{1}{A_a}\int_{\Gamma_a} \overline{\lVert\nabla\tau\rVert} dS$ |

https://doi.org/10.1371/journal.pone.0177566.t003

**Table 4. Definition of morphological indicators computed.**

| Indicator | Abbrev. | Definition used |
|---|---|---|
| *Non-sphericity index* | *NSI* | $1 - \frac{(18\pi)^{1/3} V_a^{2/3}}{A_a}$ |
| *Aspect ratio* | *AR* | $\frac{\text{Aneurysm depth}}{\text{Neck width}}$ |

https://doi.org/10.1371/journal.pone.0177566.t004

inflow velocity was adjusted to match a physiologically realistic flow rate of 245 ml/min (±61 ml/min) [33]. We matched this with an average inflow velocity of 0.27 m/s, resulting in a standard deviation of 62 ml/min. As we apply the same boundary conditions to all models, the differences in results between the models is only associated with the variations in geometry, as opposed to variations in physiological conditions, such as blood pressure or heart rate.

An average profile is obtained from elderly adults in Hoi et al. [33], measured using cine phase contrast magnetic resonance imaging (PC-MRI) at the C1 segment, with a period of 0.949 seconds (63 bpm). Since we are mainly interested in the flow in the MCA, we reduced the pulsatility by 15% to account for a dampening along the carotid siphon. The dampening has been reported to be in the range -5% to 52% with mean 17.4%. [34] The final dampened flow rate profile is visualized in Fig 2, normalized with 0.27 m/s times cross-sectional area.

On the other arteries included we used pressure conditions to approximately distribute the flow by the principle of minimum work (Murray's law) [35]. More specific, the pressure at artery $i$ is set to

$$p_i = K \left( \frac{r_i^3}{\Sigma_j r_j^3} \right)^{-1} \int_{\Gamma_i} \boldsymbol{u} \cdot \boldsymbol{n} \, dS$$

where $r_i$ denotes the radius of artery $i$, $\Gamma_i$ is the cross-sectional surface, and $\boldsymbol{n}$ the outward

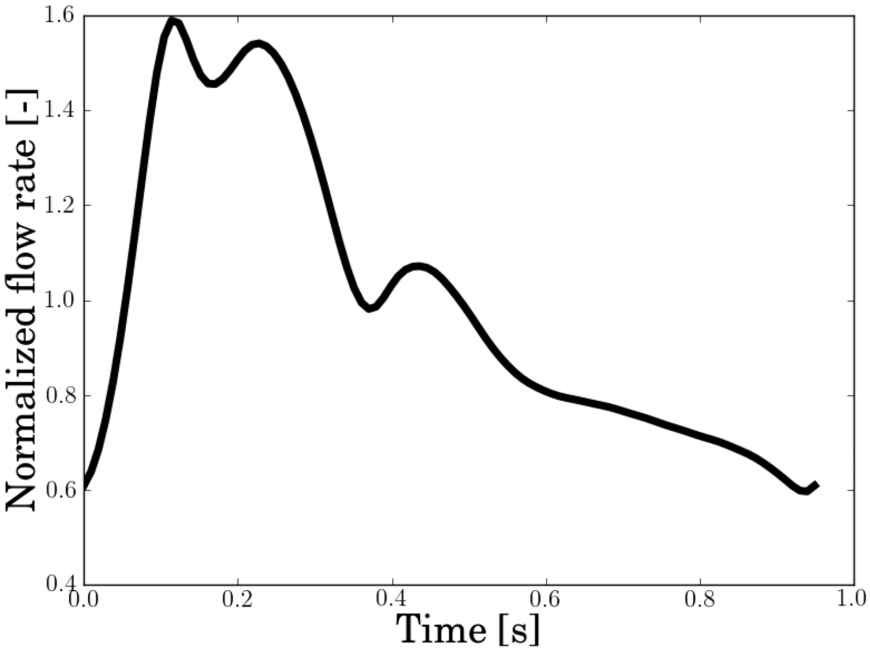


**Fig 1. The figure illustrates the differences between the coarsest resolution on the left, and the finest resolution on the right.** The clip is done just upstream from the aneurysm of model 1. The black dots represent points at which the velocity is computed.

https://doi.org/10.1371/journal.pone.0177566.g001

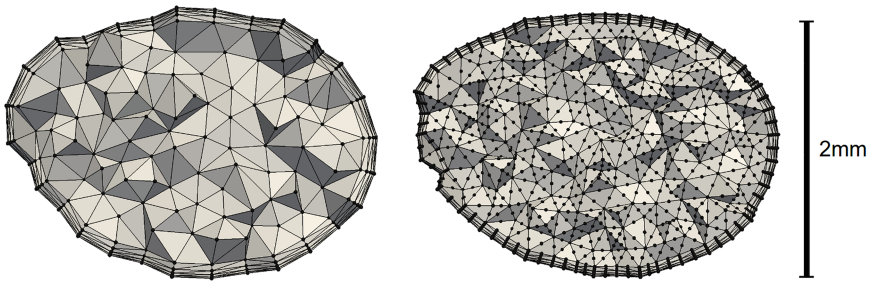


**Fig 2. Flow profile used in the simulations.**

https://doi.org/10.1371/journal.pone.0177566.g002

pointing normal. The summation is over all arteries except ICA, and the constant K is set to $10^9 \frac{kg}{m^4 s}$. This outlet condition ensures that the length of the outlets has a minimal effect on the flow division, matching Murray's law at the M2 outlets with an average deviation of -3.2% (±3.2%). These pressure conditions are preferred over velocity outflow conditions, because of the lesser influence on the upstream flow.

The incompressible Navier-Stokes equations were solved using the open source software cbcflow [36] based on FEniCS [37]. The computation of the hemodynamic indicators were done using cbcpost [38]. The solver implementation mimics very closely the one described in [39], and displays second order convergence in both time and space. The scheme is a pressure correction scheme, with a linearization of the convective term, which does not introduce artificial numerical dissipation, as shown in [40]. In fact, the numerical scheme has the same stability property as the continuous equations. At each time step, a tentative velocity is computed using the pressure field from the previous time step. This is then followed by applying the incompressibility constraint to compute a corrected pressure. Finally, the tentative velocity and corrected pressure is used to compute the final velocity.

To determine the correlation with rupture status, we first grouped the results into groups of ruptured and unruptured. We then performed a Shapiro-Wilks test for the normality of the results. Where the null hypothesis of normally distributed data could not be rejected we used a two-tailed t-test. Otherwise, we used a Mann-Whitney U-test. In addition, we performed a Bland-Altman analysis for individualized assessment of the effect of resolution.

## Results

Data from simulations of the 38 aneurysms on two different mesh refinements were analyzed. The correlation between the two sets of simulations performed is shown in Fig 3A. We see that most of the indicators are very well reproduced on the coarsest resolutions, with a few exceptions. That is, AWSS, MWSS, LSA, VDR, ICI, SCI correlate very strongly ($r>0.95$). The OSI appears to be the most difficult quantity to correctly rank, with a correlation coefficient of 0.834, which is largely caused by a few outliers. Also WSSG ($r = 0.910$) and TDWSS ($r = 0.932$) have a number of outliers. We remark that although MWSS demonstrated very strong correlation it is generally underestimated on the coarser refinement with an average deviation of 15.6%.

The variation of the hemodynamic indicators with respect to resolution is shown along the Y-axis of the logarithmic Bland-Altman plot in Fig 3B. We note that the larges variation is in LSA of up to a factor 16. Further, we note that the spread in magnitude of the different indicators for the different aneurysms (X-axis) is large in particular for WSSG, TDWSS and LSA, which is up to three orders of magnitude ($2^{11}$).

Regarding convergence, the global $L^2$-norm of the velocity varied by less than 1.2% of time-averaged velocity between the coarse and fine resolution for all aneurysms. The more thorough

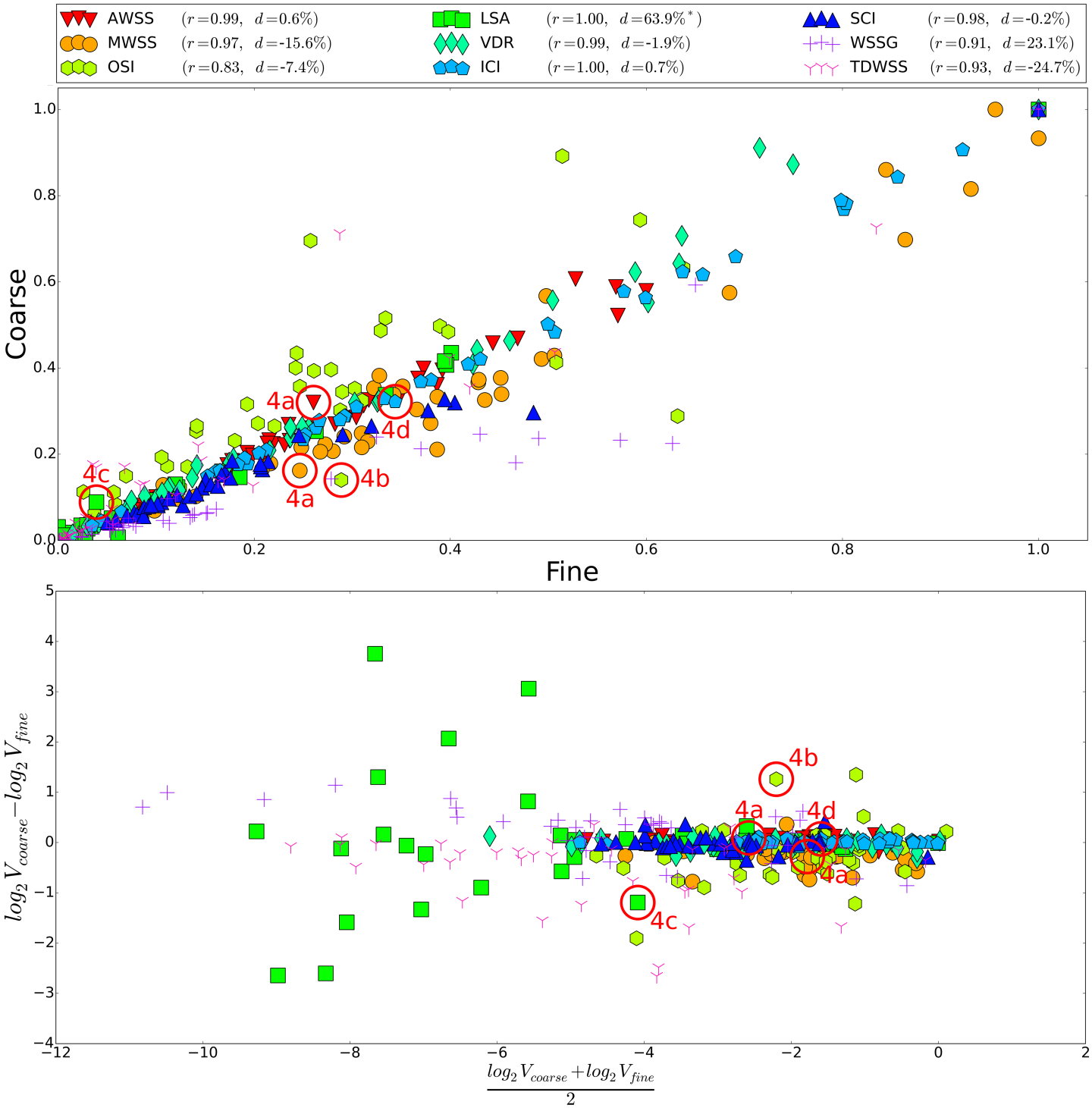


**Fig 3. Comparison between the two refinements for all hemodynamic indicators.** (A) Correlation plot between coarse and fine refinements. (B) Logarithmic Bland-Altman plot of coarse versus fine ($V_{coarse}$ *vs* $V_{fine}$). r denotes the Pearson correlation coefficient, d the average difference $\left(d = \frac{1}{38}\sum_{i=1}^{38} \frac{V^i_{coarse} - V^i_{fine}}{V^i_{fine}}\right)$. All values are normalized with the max value at the finest refinement. The red circles refer to the cases displayed in Fig 4. *: In 5 cases, LSA was zero for at least one of the two refinements (and less than 0.03 on the other). These are excluded from the Bland-Altman plot and the computation of d, to avoid division-by-zero.

https://doi.org/10.1371/journal.pone.0177566.g003

convergence test on the first five geometries, revealed a difference in the same norm of less than 0.13% between the two finest refinement levels. However, at the two finest refinement levels, the AWSS, VDR, ICI and SCI varied up to 5%. The MWSS, OSI and LSA all showed differences of up to 12%, whereas the WSSG and TDWSS showed differences of up to 40% between the two finest refinements.

Fig 4 shows a visual representation of worst case scenarios of selected indicators. Fig 4A shows the WSS at coarse and fine resolution in case 21 which is representative for the maximal difference in MWSS and AWSS. Clearly most of the main features are present in the coarse resolutions but there are spots (e.g. at the top) with clear differences. In this case, AWSS was 9.7 Pa and 8.9 Pa and MWSS 43.7 Pa and 51.8 Pa at the coarse and fine resolutions, respectively. Fig 4B shows the differences in OSI fields at coarse and fine resolution in case 48. Clearly, the coarse resolution overestimates the area of local OSI above 0.1 which results in an OSI of 0.028 at the coarse resolution and only 0.012 at the fine resolution. Fig 4C shows the LSA field in case 9, where the coarse resolution clearly underestimates the LSA. This is reflected in the values 0.033 at coarse resolution and 0.076 on the fine resolution. Finally, the ICI field for case 24 is shown in Fig 4D at t = 0.2 where only slight variations between the coarse and fine resolution can be seen. The resulting ICI is 1.20 and 1.14, respectively.

The correlation coefficients between the different indicators shown in Table 5 and Table 6 are less than the correlation between the different resolutions, which is SCI and LSA (r = 0.86). Correlation with $P<0.001$ was found between AWSS and VDR (r = 0.77), WSSG (r = 0.57), TDWSS (r = 0.53); MWSS and WSSG (r = 070); LSA and SCI (r = 0.86); WSSG and TDWSS

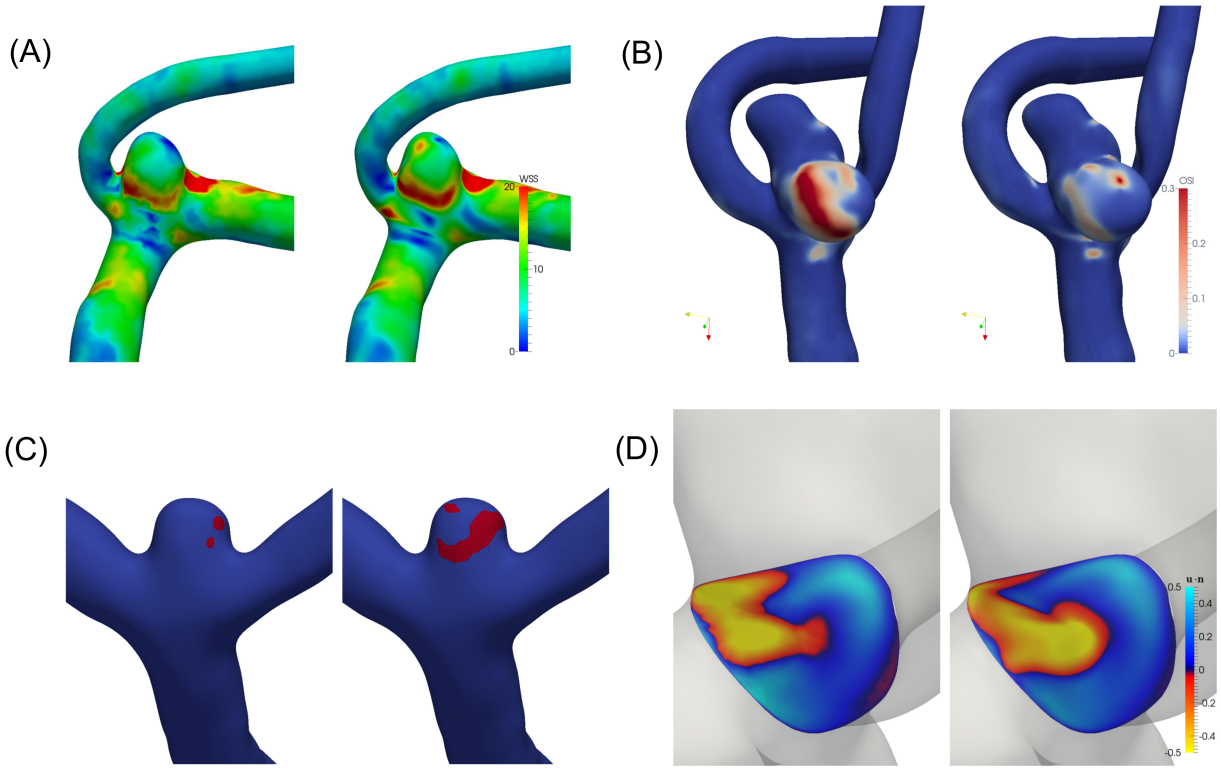


**Fig 4. Variability in selected indicators, representative of worst case.** Left figures represent the coarse resolution, right figures represent the fine. (A) Shows the WSS fields at different refinements of case 21. (Coarse/fine: AWSS = 9.7/8.9 Pa, MWSS = 43.7/51.8 Pa.) (B) OSI fields at different refinements for case 48 (coarse: 0.028, fine: 0.012). (C) LSA fields ($|\tau| < 0.1$ *in red*) at different refinements of case 9 (coarse: 0.033, fine: 0.076). (D) ICI fields at different refinements for case 24 at t = 0.2 (coarse: 1.20, fine: 1.14).

https://doi.org/10.1371/journal.pone.0177566.g004

**Table 5. Correlation coefficients between hemodynamic indicators.**

| | AWSS | MWSS | OSI | LSA | VDR | ICI | SCI | WSSG | TDWSS |
|---|---|---|---|---|---|---|---|---|---|
| *AWSS* | *1.00††* | | | | | | | | |
| *MWSS* | *0.30* | *1.00††* | | | | | | | |
| *OSI* | *-0.10* | *-0.17* | *1.00††* | | | | | | |
| *LSA* | *-0.46†* | *0.19* | *0.02* | *1.00††* | | | | | |
| *VDR* | *0.77††* | *-0.07* | *0.07* | *-0.41†* | *1.00††* | | | | |
| *ICI* | *-0.24* | *-0.33†* | *0.41†* | *-0.08* | *-0.09* | *1.00††* | | | |
| *SCI* | *-0.49†* | *0.31* | *-0.07* | *0.86††* | *-0.51†* | *-0.01* | *1.00* | | |
| *WSSG* | *0.57††* | *0.70††* | *0.00* | *-0.16* | *0.23* | *-0.33†* | *-0.12* | *1.00††* | |
| *TDWSS* | *0.53††* | *0.31* | *0.49†* | *-0.26* | *0.35†* | *0.17* | *-0.26* | *0.63††* | *1.00††* |

†: p<0.05

††: p<0.001.

https://doi.org/10.1371/journal.pone.0177566.t005

(r = 0.63). We note that OSI and ICI have no significant correlation with other indicators at this significance level. Correlation between morphological and hemodynamic indicators was P<0.001 for LSA and AR (r = 0.64); ICI and Volume (r = 0.62); SCI and AR (r = 0.62); AWSS and Volume (r = -0.55). All other correlations had P-values larger than 0.001.

Concerning rupture status, summarized in Table 7, we see that all the morphological indicators computed are able to discriminate between the two groups at a statistically significant level. Of these, NSI were the most significant, with higher values in the ruptured group (0.18 to 0.12; p = 0.007). AR was also higher in the ruptured group than in the unruptured group (1.25 to 0.97; p = 0.016). The ruptured aneurysms were also larger, demonstrated with a greater volume (123 to 88mm$^3$; p = 0.019). Of the hemodynamic indicators computed, only ICI showed a significant difference between the two groups, with higher values in the ruptured aneurysms (1.64 to 1.29; p = 0.044). MWSS also showed a tendency of higher values in the ruptured group, however not at a significant level (65.2 to 57.2; p = 0.068). The other hemodynamic indicators were not statistically significant, with p-values ranging from 0.131 to 0.896. We remark that large changes between both mesh resolutions were observed in the p-value of OSI (from 0.244 to 0.896) and MWSS (from 0.112 to 0.068). However, none of the indicators changed from not-significant to significant or vice versa with respect to resolution.

**Table 6. Correlation coefficient between all hemodynamic and morphological indicators.**

| | AR | NSI | Volume |
|---|---|---|---|
| *AWSS* | *-0.46†* | *-0.42* | *-0.55††* |
| *MWSS* | *0.29* | *0.22* | *-0.19* |
| *OSI* | *0.00* | *0.02* | *0.07* |
| *LSA* | *0.64††* | *0.43†* | *0.45†* |
| *VDR* | *-0.51†* | *-0.51†* | *-0.49†* |
| *ICI* | *0.20* | *0.35†* | *0.62††* |
| *SCI* | *0.62††* | *0.41†* | *0.51†* |
| *WSSG* | *-0.15* | *-0.18* | *-0.33†* |
| *TDWSS* | *-0.21* | *-0.11* | *-0.22* |

†: p<0.05

††: p<0.001.

https://doi.org/10.1371/journal.pone.0177566.t006

**Table 7. Comparison between the ruptured and unruptured aneurysms for all indicators at both resolutions.**

| Indicator | Units | Resolution | Ruptured | | Unruptured | | p-value |
|---|---|---|---|---|---|---|---|
| | | | Mean | Std. dev. | Mean | Std. dev. | |
| *AWSS* | *Pa* | *fine* | *6.8* | *6.3* | *7.3* | *3.9* | *0.131* |
| | | *coarse* | *7.0* | *6.5* | *7.2* | *3.9* | *0.190* |
| *MWSS* | *Pa* | *fine* | *65.2* | *32.7* | *57.2* | *44.1* | *0.068* |
| | | *coarse* | *51.8* | *24.8* | *46.3* | *30.8* | *0.112* |
| *OSI* | *-* | *fine* | *0.028* | *0.018* | *0.029* | *0.020* | *0.896* |
| | | *coarse* | *0.026* | *0.014* | *0.027* | *0.023* | *0.244* |
| *LSA* | *-* | *fine* | *0.130* | *0.238* | *0.069* | *0.114* | *0.151* |
| | | *coarse* | *0.131* | *0.234* | *0.066* | *0.109* | *0.144* |
| *VDR* | *-* | *fine* | *0.49* | *0.51* | *0.63* | *0.52* | *0.182* |
| | | *coarse* | *0.50* | *0.53* | *0.60* | *0.47* | *0.190* |
| *ICI* | *-* | *fine* | *1.64* | *0.73* | *1.29* | *0.98* | ***0.044*** |
| | | *coarse* | *1.66* | *0.74* | *1.30* | *0.98* | ***0.041*** |
| *SCI* | *-* | *fine* | *6.9* | *8.2* | *4.5* | *2.7* | *0.295* |
| | | *coarse* | *6.4* | *6.7* | *4.6* | *2.9* | *0.306* |
| *WSSG* | *Pa/mm* | *fine* | *1012* | *1202* | *2138* | *3368* | *0.137* |
| | | *coarse* | *1154* | *1516* | *1861* | *2093* | *0.124* |
| *TDWSS* | *Pa/s* | *fine* | *407* | *729* | *400* | *541* | *0.235* |
| | | *coarse* | *315* | *577* | *260* | *401* | *0.244* |
| *AR* | *-* | *-* | *1.25* | *0.43* | *0.97* | *0.41* | ***0.016*** |
| *NSI* | *-* | *-* | *0.18* | *0.05* | *0.12* | *0.07* | ***0.007*** |
| *Volume* | *$mm^3$* | *-* | *123* | *95* | *88* | *143* | ***0.019*** |

https://doi.org/10.1371/journal.pone.0177566.t007

## Discussion

In this study we investigated the computational robustness of hemodynamic indicators based on two of the most frequently cited quantitative studies in the field [10,14], on a dataset consisting of 25 unruptured and 13 ruptured MCA aneurysms. In addition, we included three common morphological indicators, as well as two hemodynamic indicators for completeness. Coarse and fine resolution simulations correlated very strongly ($r>0.95$) for AWSS, MWSS, LSA, VDR, ICI, SCI, while OSI ($r = 0.83$), WSSG ($r = 0.91$), and TDWSS ($r = 0.93$) correlated strongly. Although strongly correlated, the important deviations from the identity line observed for LSA (d = 63.9%), TDWSS (d = -24.7%) and WSSG (d = 23.1%) indicates over- or underestimation in the coarser resolution with respect the finer resolution. The inspection of the corresponding logarithmic Bland-Altman plot revealed large variations for the lower values, in particular for LSA. The variation of up to 16 ($2^4$) demonstrates that correlation alone is not a sufficient criterion for robustness. From the plot, we see that LSA, WSSG, TDWSS in particular are difficult to accurately compute for lower values.

Our coarse resolution in this study is representative of a normal or high resolution in common CFD analysis of aneurysms. Considering the global $L^2$-norm of the velocity, we found only very small changes ($<1.2\%$) between this resolution and our finest resolution. However, even at the finest refinement levels, a detailed convergence analysis of the indicators on five aneurysms showed that not all indicators were converged in the strict sense usually applied to CFD analysis. Only the indicators AWSS, VDR, ICI, and SCI showed a differences of less than 5% between the two finest refinements. MWSS, OSI and LSA showed differences of up to 12%, while WSSG and TDWSS had a difference of up to 40%. Note that as the mesh resolution

change, the approximation of the wall geometry also changed slightly. This might contribute to the lack of convergence of several indicators.

Correlation between indicators were weak to none, with the exception of SCI-LSA (r = 0.86), VDR-AWSS (r = 0.77), WSSG-MWSS (r = 0.70), and TWDSS-WSSG (r = 0.63). Correlation between morphological and hemodynamic indicators were weak to none except for LSA-AR (r = 0.64), SCI-AR (r = 0.62), and ICI-Volume (r = 0.62). This suggests that there could be possibilities for surrogates that are more robust, for example the SCI as a surrogate for the less robust LSA.

Only one of the hemodynamic indicators, the ICI, showed a significant difference between ruptured and unruptured aneurysms. The morphological indicators all showed significant differences between the two groups, with NSI as the strongest of the three indicators included. For the other hemodynamic indicators, the tendencies were as expected with basis in the studies they were taken from, but not strong enough to reach statistical significance. The OSI was however an exception from this, where the means were practically identical, and the p-value as high as 0.896. For MWSS, the tendency was towards *higher* MWSS in ruptured aneurysms than unruptured aneurysms, but with a p-value of 0.068, this was not deemed significant. The increased resolution did not change the p-value from significant to not-significant or vice versa for any of the indicators. This suggests that coarse simulations can provide useful information, even though the actual values are not strictly converged.

This study involved 38 MCA aneurysms which is less than the 119 and 210 in Cebral et al. [10] and Xiang et al. [14] and might explain why statistical significance was not obtained. We have also only studied MCA bifurcation aneurysms, which may have different mechanisms related to rupture than aneurysms at other locations. Still, from the coefficient of variation (standard deviation divided by mean) of 0.5–1.83 in Table 7, we can conclude that the hemodynamic variations within aneurysms at this location are substantial. In addition, this study, as comparable studies, is done retrospectively. This further complicates the usage of these indicators as predictors of aneurysm rupture. In particular, it has been shown that the morphology may be significantly affected by aneurysm rupture [41]. Finally, we remark that we have not assumed laminar flow in our simulations and our numerical algorithms were hence not tailored towards such application, using e.g. dissipative or stabilized schemes. The results in particular for OSI, WSSG and TDWSS might have been different if laminar flow was assumed.

The spatial resolution of the quantitative studies considered in [10] and [14] are similar to what we consider coarse resolution. Xiang et al. [14] report 300 000 to 1 000 000 tetrahedral elements, with a hexahedral boundary layer, whereas Cebral et al. [10] report a resolution of 0.1 to 0.2 mm. The temporal resolution is typically much coarser than what we have used, with time steps of 0.001s to 0.01s [19]. This is connected to the solution strategy as mentioned above, an implicit or explicit assumption of laminar flow, and the usage of diffusive schemes or stabilization terms. Other relevant studies such as [12,42–44] either lack information about resolution, or report similar resolutions. In light of the results in this study and recent studies such as [19,22], it seems reasonable to question whether these results are converged in a strict sense. However, using quantitative methods, the results of this study suggest that strict convergence does not alter conclusions based on quantitative analysis.

A detailed grid convergence of 5 aneurysms was done by Hodis et al. [45], where the authors used extrapolation to estimate the grid uncertainty of velocities and average and maximal WSS at peak systole. Our meshes are roughly comparable to their mesh refinements $h_4$ and $h_1$. They reported grid convergence errors in average WSS of 1–11% and in maximal WSS of 6–15% for the finest mesh. This does not compare directly to our findings, but similar to this study, it highlights the difficulties of strict convergence. They state that each patient-specific model requires individual grid convergence studies. However, as our study shows, this

requirement might be unnecessary strict for quantitative studies that considers tens to hundreds of aneurysm models, as the effect of outliers will be diminished.

In Khan et al. [22], the authors study resolution requirements on 3 different aneurysms. They highlight the need for a minimally dissipative solver as more important than grid or temporal resolution. In this study we use the same numerical scheme as the high fidelity solver used by the authors in that study. They state that this high fidelity solver "can tolerate surprisingly coarse resolutions", and show that in particular AWSS and OSI are properly resolved at spatial resolutions comparable to our coarse resolutions. In our study, we find that for our 38 cases, this still holds true for AWSS, but the OSI seems more difficult to resolve for certain geometries.

## Conclusion

In this study we demonstrate that a quantitative CFD analysis of hemodynamics in cerebral aneurysms, are reasonably robust even though strict convergence in a traditional sense is not obtained. This suggests that the results of the previous quantitative CFD studies such as [10,12,14,40–42], would correlate strongly with properly resolved simulations, although we note that our simulations and scheme may not be representative for all previous studies, which often employ dissipative schemes. However, some hemodynamic indicators such as AWSS, VDR, ICI and SCI are relatively easy to resolve, compared to OSI, LSA, MWSS, WSSG and TDWSS. For individual assessment, special care should be taken that the considered hemodynamic indicators are converged, as there are outliers. Besides ICI, the hemodynamic parameters studied here were unable to discriminate ruptured from unruptured aneurysms.

## Supporting information

**S1 Fig. Geometries.** All geometries used in our computations. Scale is not equal for all images.
(TIFF)

**S1 Table. A short, but specific definition of the different values used to compute the hemodynamic indicators.** The near-vessel domain is defined as the distance from the aneurysm neck of less than 1cm (shortest path, computed using Dijkstra's algorithm).
(DOCX)

## Acknowledgments

The simulations performed in this study was done on the Abel Cluster (project NN9279K), owned by the University of Oslo and the Norwegian metacenter for High Performance Computing (NOTUR), and operated by the Department for Research Computing at USIT, the University of Oslo IT-department. http://www.hpc.uio.no/. An approximate total of 250 000 CPU hours were spent on the simulations for this study.

## Author Contributions

**Conceptualization:** ØE AFF KAM JMP.

**Data curation:** AFF JMP.

**Formal analysis:** ØE AFF KAM JMP.

**Funding acquisition:** KAM AFF.

**Investigation:** ØE AFF KAM JMP.

**Methodology:** ØE AFF KAM JMP.

**Project administration:** AFF KAM.

**Resources:** KAM.

**Software:** ØE KAM.

**Supervision:** AFF KAM.

**Validation:** ØE KAM.

**Visualization:** ØE.

**Writing – original draft:** ØE KAM.

**Writing – review & editing:** ØE AFF KAM JMP.

## References


1. Rinkel GJE, Djibuti M, Algra A, van Gijn J. Prevalence and risk of rupture of intracranial aneurysms: A systematic review. Stroke. 1998; 29: 251–256. https://doi.org/10.1161/01.STR.29.1.251 PMID: 9445359
2. Hop JW, Rinkel GJE, Algra A, van Gijn J. Case-Fatality Rates and Functional Outcome After Subarachnoid Hemorrhage: A Systematic Review. Stroke. 1997; 28: 660–664. https://doi.org/10.1161/01.STR.28.3.660 PMID: 9056628
3. Weir B, Amidei C, Kongable G, Findlay JM, Kassell NF, Kelly J, et al. The aspect ratio (dome/neck) of ruptured and unruptured aneurysms. J Neurosurg. 2003; 99: 447–451. https://doi.org/10.3171/jns.2003.99.3.0447 PMID: 12959428
4. Raghavan ML, Ma B, Harbaugh RE. Quantified aneurysm shape and rupture risk. J Neurosurg. 2005; 102: 355–362. https://doi.org/10.3171/jns.2005.102.2.0355 PMID: 15739566
5. Millán RD, Dempere-Marco L, Pozo JM, Cebral JR, Frangi AF. Morphological characterization of intracranial aneurysms using 3-D moment invariants. IEEE Trans Med Imaging. 2007; 26: 1270–1282. https://doi.org/10.1109/TMI.2007.901008 PMID: 17896598
6. Dhar S, Tremmel M, Mocco J, Kim M, Yamamoto J, Siddiqui AH, et al. Morphology parameters for intracranial aneurysm rupture risk assessment. Neurosurgery. 2008; 63: 185–197. https://doi.org/10.1227/01.NEU.0000316847.64140.81 PMID: 18797347
7. Valencia C, Villa-Uriol MC, Pozo JM, Frangi AF. Morphological descriptors as rupture indicators in middle cerebral artery aneurysms. Engineering in Medicine and Biology Society (EMBC), 2010 Annual International Conference of the IEEE. 2010. pp. 6046–6049. 10.1109/IEMBS.2010.5627610
8. Lauric A, Miller EL, Baharoglu MI, Malek AM. 3D shape analysis of intracranial aneurysms using the Writhe number as a discriminant for rupture. Ann Biomed Eng. 2011; 39: 1457–1469. https://doi.org/10.1007/s10439-010-0241-x PMID: 21225345
9. Cebral JR, Mut F, Weir J, Putman CM. Association of hemodynamic characteristics and cerebral aneurysm rupture. Am J Neuroradiol. Am Soc Neuroradiology; 2011; 32: 264–270. https://doi.org/10.3174/ajnr.A2274 PMID: 21051508
10. Cebral JR, Mut F, Weir J, Putman C. Quantitative characterization of the hemodynamic environment in ruptured and unruptured brain aneurysms. Am J Neuroradiol. Am Soc Neuroradiology; 2011; 32: 145–151. https://doi.org/10.3174/ajnr.A2419 PMID: 21127144
11. Qian Y, Takao H, Umezu M, Murayama Y. Risk analysis of unruptured aneurysms using computational fluid dynamics technology: preliminary results. AJNR Am J Neuroradiol. 2011; 32: 1948–1955. https://doi.org/10.3174/ajnr.A2655 PMID: 21903914
12. Takao H, Murayama Y, Otsuka S, Qian Y, Mohamed A, Masuda S, et al. Hemodynamic differences between unruptured and ruptured intracranial aneurysms during observation. Stroke. 2012; 43: 1436–1439. https://doi.org/10.1161/STROKEAHA.111.640995 PMID: 22363053
13. Miura Y, Ishida F, Umeda Y, Tanemura H, Suzuki H, Matsushima S, et al. Low wall shear stress is independently associated with the rupture status of middle cerebral artery aneurysms. Stroke. 2013; 44: 519–521. https://doi.org/10.1161/STROKEAHA.112.675306 PMID: 23223503
14. Xiang J, Natarajan SK, Tremmel M, Ma D, Mocco J, Hopkins LN, et al. Hemodynamic-morphologic discriminants for intracranial aneurysm rupture. Stroke. 2011; 42: 144–152. https://doi.org/10.1161/STROKEAHA.110.592923 PMID: 21106956

15. Kallmes DF. Point: CFD—computational fluid dynamics or confounding factor dissemination. Am J Neuroradiol. 2012; 33: 395–6. https://doi.org/10.3174/ajnr.A2993 PMID: 22268081

16. Steinman DA, Hoi Y, Fahy P, Morris L, Walsh MT, Aristokleous N, et al. Variability of computational fluid dynamics solutions for pressure and flow in a giant aneurysm: The ASME 2012 Summer Bioengineering Conference CFD Challenge. J Biomech Eng. American Society of Mechanical Engineers; 2013; 135: 21016–21016–13. https://doi.org/10.1115/1.4023382 PMID: 23445061

17. Valen-Sendstad K, Mardal K-A, Mortensen M, Reif BAP, Langtangen HP. Direct numerical simulation of transitional flow in a patient-specific intracranial aneurysm. J Biomech. 2011; 44: 2826–2832. https://doi.org/10.1016/j.jbiomech.2011.08.015 PMID: 21924724

18. Valen-Sendstad K, Mardal K-A, Steinman DA. High-resolution CFD detects high-frequency velocity fluctuations in bifurcation, but not sidewall, aneurysms. J Biomech. 2013; 46: 402–407. https://doi.org/10.1016/j.jbiomech.2012.10.042 PMID: 23174422

19. Valen-Sendstad K, Steinman DA. Mind the gap: Impact of computational fluid dynamics solution strategy on prediction of intracranial aneurysm hemodynamics and rupture status indicators. Am J Neuroradiol. 2013; 35: 536–543. https://doi.org/10.3174/ajnr.A3793 PMID: 24231854

20. Ventikos Y. Resolving the issue of resolution. AJNR Am J Neuroradiol. 2014; 35: 544–545. https://doi.org/10.3174/ajnr.A3894 PMID: 24503558

21. Jain K, Roller S, Mardal K-A. Transitional flow in intracranial aneurysms-A space and time refinement study below the Kolmogorov scales using Lattice Boltzmann Method. Comput Fluids. 2016; 127: 36–46. https://doi.org/10.1016/j.compfluid.2015.12.011

22. Khan MO, Valen-Sendstad K, Steinman DA. Narrowing the expertise gap for predicting intracranial aneurysm hemodynamics: Impact of solver numerics versus mesh and time-step resolution. Am J Neuroradiol. 2015; 36: 1310–1316. https://doi.org/10.3174/ajnr.A4263 PMID: 25742983

23. Villa-Uriol MC, Berti G, Hose DR, Marzo A, Chiarini A, Penrose J, et al. @neurIST complex information processing toolchain for the integrated management of cerebral aneurysms. Interface Focus. 2011; 1: 308–319. https://doi.org/10.1098/rsfs.2010.0033 PMID: 22670202

24. The @neurIST Integrated Project. In: http://www.aneurist.org. Accessed on July 7, 2016. [Internet]. Available: http://www.aneurist.org

25. Bogunović H, Pozo JM, Villa-Uriol MC, Majoie C, van den Berg R, Gratama van Andel HAF, et al. Automated segmentation of cerebral vasculature with aneurysms in 3DRA and TOF-MRA using geodesic active regions: An evaluation study. Med Phys. 2011; 38: 210–222. https://doi.org/10.1118/1.3515749 PMID: 21361189

26. Valen-Sendstad K, Piccinelli M, Steinman DA. High-resolution computational fluid dynamics detects flow instabilities in the carotid siphon: Implications for aneurysm initiation and rupture? J Biomech. 2014; 47: 3210–3216. https://doi.org/10.1016/j.jbiomech.2014.04.018 PMID: 25062933

27. Ujiie H, Tachibana H, Hiramatsu O, Hazel AL, Matsumoto T, Ogasawara Y, et al. Effects of size and shape (aspect ratio) on the hemodynamics of saccular aneurysms: a possible index for surgical treatment of intracranial aneurysms. Neurosurgery. 1999; 45: 119–129. https://doi.org/10.1097/00006123-199907000-00028 PMID: 10414574

28. Cebral JR, Mut F, Weir J, Putman CM. Association of hemodynamic characteristics and cerebral aneurysm rupture. Am J Neuroradiol. Am Soc Neuroradiology; 2011; 32: 264–270. https://doi.org/10.3174/ajnr.A2274 PMID: 21051508

29. Bland JM, Altman DG. Measuring agreement in method comparison studies. Stat Methods Med Res. 1999; 8: 135–160. https://doi.org/10.1177/096228029900800204 PMID: 10501650

30. Evju Ø, Valen-Sendstad K, Mardal K-A. A study of wall shear stress in 12 aneurysms with respect to different viscosity models and flow conditions. J Biomech. 2013; 46: 2802–2808. https://doi.org/10.1016/j.jbiomech.2013.09.004 PMID: 24099744

31. Womersley JR. Method for the calculation of velocity, rate of flow and viscous drag in arteries when the pressure gradient is known. J Physiol. 1955; 127: 553–563. https://doi.org/10.1113/jphysiol.1955.sp005276 PMID: 14368548

32. Valen-Sendstad K, Piccinelli M, KrishnankuttyRema R, Steinman DA. Estimation of inlet flow rates for image-based aneurysm CFD models: Where and how to begin? Ann Biomed Eng. 2015; 43: 1422–1431. https://doi.org/10.1007/s10439-015-1288-5 PMID: 25707596

33. Hoi Y, Wasserman B a, Xie YJ, Najjar SS, Ferruci L, Lakatta EG, et al. Characterization of volumetric flow rate waveforms at the carotid bifurcations of older adults. 2011; 31: 291–302. doi: 10.1088/0967-3334/31/3/002. Characterization PMID: 20086276

34. Schubert T, Santini F, Stalder a. F, Bock J, Meckel S, Bonati L, et al. Dampening of blood-flow pulsatility along the carotid siphon: Does form follow function? AJNR Am J Neuroradiol. 2011; 32: 1107–1112. https://doi.org/10.3174/ajnr.A2426 PMID: 21474624

35. Sherman TF. On connecting large vessels to small. The meaning of Murray's law. J Gen Physiol. 1981; 78: 431–453. https://doi.org/10.1085/jgp.78.4.431 PMID: 7288393

36. Evju Ø, Alnæs MS. cbcflow [Internet]. 2016. Available: https://bitbucket.org/simula_cbc/cbcflow

37. Logg A, Mardal K-A, Wells G. Automated solution of differential equations by the finite element method: The FEniCS book. Springer Science & Business Media; 2012. https://doi.org/10.1007/978-3-642-23099-8

38. Evju Ø, Alnæs MS. cbcpost [Internet]. 2016. Available: https://bitbucket.org/simula_cbc/cbcpost

39. Mortensen M, Valen-Sendstad K. Oasis: A high-level/high-performance open source Navier–Stokes solver. Comput Phys Commun. 2015; 188: 177–188. https://doi.org/10.1016/j.cpc.2014.10.026

40. Simo JCC, Armero F. Unconditional stability and long-term behavior of transient algorithms for the incompressible Navier-Stokes and Euler equations. Comput Methods Appl Mech Eng. Elsevier; 1994; 111: 111–154. https://doi.org/10.1016/0045-7825(94)90042-6

41. Schneiders JJ, Marquering H a., Van Den Berg R, VanBavel E, Velthuis B, Rinkel GJE, et al. Rupture-associated changes of cerebral aneurysm geometry: High-resolution 3D imaging before and after rupture. Am J Neuroradiol. 2014; 35: 1358–1362. https://doi.org/10.3174/ajnr.A3866 PMID: 24557706

42. Jou L-D, Lee DH, Morsi H, Mawad ME. Wall shear stress on ruptured and unruptured intracranial aneurysms at the internal carotid artery. Am J Neuroradiol. 2008; 29: 1761–1767. https://doi.org/10.3174/ajnr.A1180 PMID: 18599576

43. Retarekar R. Hemodynamics and natural history outcome in unruptured intracranial aneurysms [Internet]. University of Iowa. 2012. Available: http://ir.uiowa.edu/etd/3520/

44. Xiang J, Yu J, Choi H, Dolan Fox JM, Snyder K V, Levy EI, et al. Rupture Resemblance Score (RRS): Toward risk stratification of unruptured intracranial aneurysms using hemodynamic-morphological discriminants. J Neurointerv Surg. 2015; 7: 490–495. https://doi.org/10.1136/neurintsurg-2014-011218 PMID: 24811740

45. Hodis S, Uthamaraj S, Smith AL, Dennis KD, Kallmes DF, Dragomir-Daescu D. Grid convergence errors in hemodynamic solution of patient-specific cerebral aneurysms. J Biomech. 2012; 45: 2907–2913. https://doi.org/10.1016/j.jbiomech.2012.07.030 PMID: 23062796